A&A 627, A79 (2019)
https://doi.org/10.1051/0004-6361/201935119

Astronomy & Astrophysics

Derivation of the physical parameters of the jet in S5 0836+710 from stability analysis

L. Vega-García[1], M. Perucho[2,3], and A. P. Lobanov[1,4]

[1] Max-Planck-Institut für Radioastronomie, Auf dem Hügel 69, 53121 Bonn, Germany
e-mail: lauvegar@mpifr-bonn.mpg.de
[2] Departament d'Astronomia i Astrofísica, Universitat de València, C/ Dr. Moliner, 50, 46100 Burjassot, València, Spain
e-mail: manel.perucho@valencia.edu
[3] Observatori Astronòmic, Universitat de València, C/ Catedràtic Beltrán 2, 46091 Paterna, València, Spain
[4] Institut für Experimentalphysik, Universität Hamburg, Luruper Chaussee 149, 22761 Hamburg, Germany

Received 23 January 2019 / Accepted 29 March 2019

ABSTRACT

Context. A number of extragalactic jets show periodic structures at different scales that can be associated with growing instabilities. The wavelengths of the developing instability modes and their ratios depend on the flow parameters, so the study of those structures can shed light on jet physics at the scales involved.
Aims. In this work, we use the fits to the jet ridgeline obtained from different observations of S5 B0836+710 and apply stability analysis of relativistic, sheared flows to derive an estimate of the physical parameters of the jet.
Methods. Based on the assumption that the observed structures are generated by growing Kelvin–Helmholtz (KH) instability modes, we ran numerical calculations of stability of a relativistic, sheared jet over a range of different jet parameters. We spanned several orders of magnitude in jet-to-ambient medium density ratio, and jet internal energy, and checked different values of the Lorentz factor and shear layer width. This represents an independent method to obtain estimates of the physical parameters of a jet.
Results. By comparing the fastest growing wavelengths of each relevant mode given by the calculations with the observed wavelengths reported in the literature, we have derived independent estimates of the jet Lorentz factor, specific internal energy, jet-to-ambient medium density ratio, and Mach number. We obtain a jet Lorentz factor $\gamma \simeq 12$, specific internal energy of $\varepsilon \simeq 10^{-2}\,c^2$, jet-to-ambient medium density ratio of $\eta \sim 10^{-3}$, and an internal (classical) jet Mach number of $M_{\rm j} \sim 12$. We also find that the wavelength ratios are better recovered by a transversal structure with a width of ≃10% of the jet radius.
Conclusions. This method represents a powerful tool to derive the jet parameters in all jets showing helical patterns with different wavelengths.

Key words. galaxies: jets – magnetohydrodynamics (MHD) – quasars: individual: S5 0836+710 – radio continuum: galaxies – relativistic processes

1. Introduction

Extragalactic jets of relativistic plasma are formed in the immediate vicinity of supermassive black holes (SMBH) residing in the nuclei of active galaxies (AGN, Blandford & Znajek 1977). The jets not only carry energy from this region to hundreds of kiloparsecs, but also condition galaxy evolution from the moment they are initially triggered (see, e.g., McNamara & Nulsen 2012). Therefore, determination of their physical parameters can allow us to understand the precise processes governing them and understand their impact on the ambient medium in more detail.

Radio images of many extragalactic jets from AGN show helical patterns on parsec and kiloparsec scales (see, e.g., Lister et al. 2013). In different works, these patterns have been associated either with Alfvén (Cohen et al. 2015) or with pressure waves (Perucho et al. 2012a). A periodicity in the direction of ejection of the flow due to jet precession is probably the origin of the oscillations. Precession can arise from the gravitational effect of the accretion disk on the compact object in the center of the AGN or in a binary black hole (see, e.g., Lister et al. 2003; Stirling et al. 2003; Lobanov & Roland 2005; Bach et al. 2006; Savolainen et al. 2006). Once triggered, the induced oscillation can couple to instability modes of the Kelvin–Helmholtz instability (KH, Perucho et al. 2005, 2010; Mizuno et al. 2007) or current driven instability (CD, Mizuno et al. 2009, 2011; McKinney & Blandford 2009; Mignone et al. 2010) and grow in amplitude with time or distance as the wave is advected downstream.

The radio source S5 0836+710 (4C +71.07; J0841+7053) is a powerful low-polarization quasar (LPQ) located at a redshift of 2.17 (Osmer et al. 1994), which corresponds to the luminosity distance of 16.9 Gpc and a linear scale of 8.4 pc mas^{-1}, assuming the standard Lambda-cold dark matter (ΛCDM) cosmology ($H_0 = 73\,{\rm km\,s^{-1}\,Mpc^{-1}}$, $\Omega_{\rm m} = 0.27$, $\Omega_\Lambda = 0.73$) (Planck Collaboration XIII 2016). It has a long and one-sided jet at parsec and kiloparsec scales.

Large-scale radio emission was revealed by the VLA[1] and MERLIN[2] at distances larger than 1 arcsecond (Hummel et al. 1992; Perucho et al. 2012b). The jet shows apparent speeds of up to 21 c at 15 GHz, with a mean of 17 c ($\gamma_{\rm j} \simeq 17$), as reported by Lister et al. (2013). The estimated jet viewing angle is $\theta \approx 3.2°$

[1] *Karl G. Jansky* Very Large Array of the National Radio Astronomy Observatory, Socorro, NM, USA.
[2] Multi-Element Radio Linked Interferometer Network of the Jodrell Bank Observatory, UK.

as estimated by Otterbein et al. (1998), who also gave a Lorentz factor of $\gamma_j = 12$ from jet kinematics at 8 GHz.

The source morphology suggests the existence of plasma instability. Krichbaum et al. (1990) observed the source with VLBI[3] at 326 MHz and 5 GHz and recognized several kinks in the flow that can be associated with the growth of instability. From high-resolution images obtained with VLBI Space Observatory Program (VSOP; Hirabayashi et al. 2000) at 1.6 GHz and 5 GHz, Lobanov et al. (1998) suggested the presence of KH instability in the flow, based on the observed morphology of the jet brightness ridgeline. The oscillations in the ridgeline were identified with helical and elliptical surface modes of the instability. Perucho et al. (2012a) provided further evidence for the interpretation of these oscillations as caused by KH instability modes. Furthermore, observations with MERLIN show an emission gap between 0.2″ and 1.0″ and a large-scale, apparently decollimated structure beyond 1″. This was explained as the expansion and disruption of the jet due to a helical instability mode (Perucho et al. 2012b).

In this paper, we use the results obtained from different observational campaigns on this source (see Lobanov et al. 2006; Perucho et al. 2012a), complemented by the Global VLBI array observations performed on October 24, 2013, (*L*-Band), as part of RadioAstron space VLBI observations of S5 0836+710 (Vega García 2018; Vega García et al. 2019). We apply a numerical solver of the stability equation for sheared, relativistic flows (Perucho et al. 2007; Perucho & Lobanov 2007) to derive an estimate of the physical parameters in the jet. In contrast with Perucho & Lobanov (2007), where the authors fixed the physical parameters of the jet to those obtained via previous estimates (Lobanov et al. 1998, 2006) and studied the possibility of the presence of a shear layer separating the jet and its environment, here we provide an independent estimate of all the relevant parameters without any initial restriction. The wavelengths corresponding to the fastest growing modes derived from the calculations are compared to the observed wavelengths in the jet, which allows us to provide a set of jet parameters.

The paper is structured as follows. In Sect. 2 we summarize the observational results that have provided fits to the intrinsic wavelengths of the jet ridgeline. Section 3 includes an explanation of the method that we have used. The results obtained are presented in Sect. 4. Finally, the discussion of those results and conclusions of this work are given in Sect. 5.

2. Ridgeline oscillations

The ridgeline of the jet is defined as a line connecting the maxima of Gaussian profiles fitted to the jet brightness profiles measured transversally to the jet direction. Figure 1 shows an example of the ridgeline in the jet in 0836+710 from a VLBI image at 1.6 GHz (Vega García 2018; Vega García et al. 2019). At this frequency, the jet in 0836+710 can be traced up to ∼130 mas (deprojected linear distance of ∼10 kpc), which enables the making of detailed studies of a number of instability wavelengths.

A comparison of the ridgelines obtained from the VLBI images of 0836+710 made at 1.6 GHz at different epochs shows a consistent picture of a slowly evolving instability pattern in the jet (Perucho et al. 2012a). These ridgelines are shown in Fig. 2, tracing the jet up to a distance of 65 mas. At distances larger than about 60 mas, the jet is substantially resolved in the transverse direction. At these scales the formal ridgeline derived from the brightness profiles is not as reliable for reflecting the

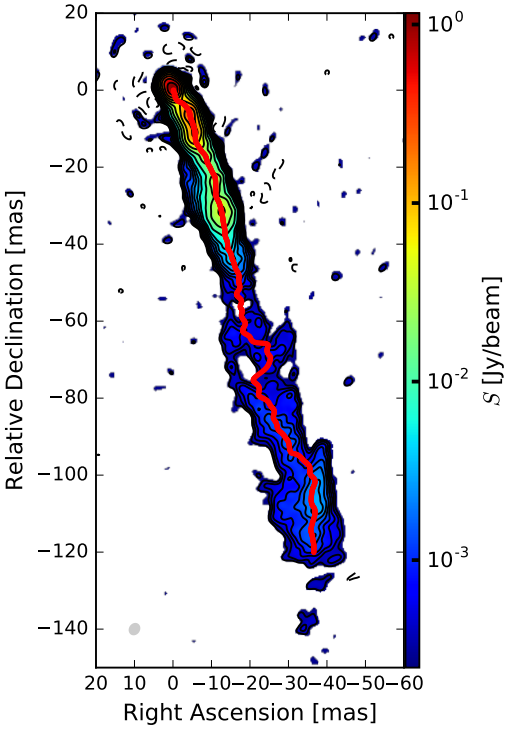

Fig. 1. Ridgeline (red) for ground-VLBI observations at 1.6 GHz. The contour levels are drawn at $(-1, 1, \sqrt{2}, 2, \ldots)$ times 0.32 mJy beam^{-1}. These data are from Vega García (2018), Vega García et al. (2019).

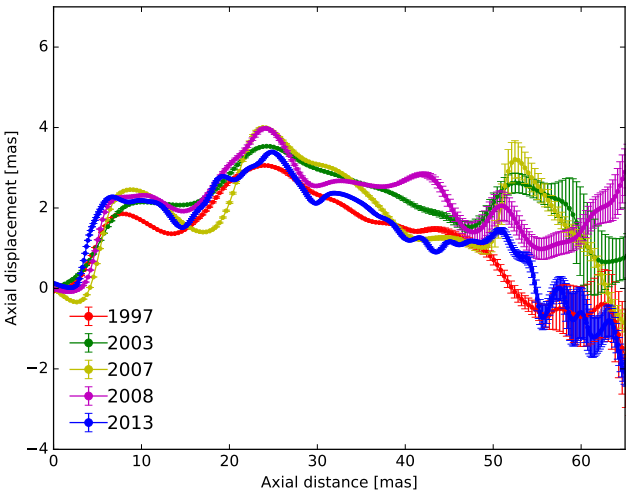

Fig. 2. Ridgelines at 1.6 GHz from the observations described in Perucho et al. (2012a) together with those derived from the 2013/2014 Global VLBI observations. The main described structure is similar. The differences are due to the time difference, different data quality, and different uv-coverages.

plasma instability development, and a more complex description comprising multiple threads inside the flow may be needed (e.g., the one similar to the approach employed for strongly resolved jets in 3C273; Lobanov & Zensus 2001). In addition to this, it is also likely that the plasma instability modes developing in the inner jet would saturate or dissipate at these distances (see Perucho et al. 2012a). Because of these considerations, we limit our analysis of the jet instability in 0836+710 to the structures traced by the jet ridgeline within the inner 65 mas of the flow. The ridgelines offsets are plotted with respect to

[3] Very Long Baseline Interferometry.

the overall jet axis assumed to be oriented at a position angle of −162°. The small differences observed among the different epochs can be attributed to image noise and small changes in time (Perucho et al. 2012a; Vega García 2018).

Since the oscillations displace the jet axis from a straight line (as expected for the helical modes of KH instability) and the transverse profiles show hints of double-peaked structure (expected for the elliptical mode of the instability) only in the close vicinity of the core (Perucho et al. 2012a), we consider that helical modes are largely determining the appearance of the ridgelines. The oscillations can thus be modeled as waves developing along the jet. From now on, we assume that these waves correspond to KH instability modes developing in the jet. Therefore, one can take the offset of the ridge from the straight line defining the jet direction as the projected amplitude of the wave, $\Delta r(z)$. Taking into account that the jet opening angle is small (<1°, Perucho et al. 2012a), the expected effect of jet expansion on the mode wavelength ($\lambda \propto R$, Hardee 1982) can be considered to be small. Then, assuming a constant wave amplitude[4], the offsets can be modeled as

$$\Delta r(z) = \sum_{i=1}^{N_{\rm mod}} a_i \sin(2\pi/\lambda_i + \psi_i)\,, \tag{1}$$

where a_i is the amplitude, ψ_i the phase, and λ_i the wavelength corresponding to the i-th mode. The offsets of the ridge on the plane of the sky are not affected by projection effects. However, taking into account that we model a three-dimensional helical structure, there is a distortion on the observed ridgeline produced by travel time effects across the jet cross section. In this case, the distortion is caused by the oscillation in the direction orthogonal to both the jet axis and the direction defined by the observed ridgeline ripples on the plane of the sky. Our approach neglects the role of that distortion because we focus on the longest wavelengths ($\lambda \gg R_{\rm j}$), where these distortions are less relevant than for shorter ones ($\lambda \sim R_{\rm j}$).

The χ^2 fits to the ridges can be done in two different ways: either by fitting one mode at a time and subtracting it from the original ridgeline before fitting the next mode, or by fitting all modes simultaneously, starting from an initial set of mode parameters determined in earlier works (e.g., Lobanov et al. 2006; Perucho et al. 2012a). Both approaches give the same results (see, e.g., Vega García 2018 for the fits to the ridgline of the Global VLBI 1.6 GHz image of the source). For the purposes of this work, we only need the result of this fit, which is reproduced in Table 1. It is important to stress that the wavelengths obtained by this analysis are similar to those derived in previous works (Lobanov et al. 2006; Perucho et al. 2012a), with improved resolution in our case since the observations included the Global VLBI array.

It is interesting to stress that the shorter wavelengths (~35, 16.5, 6.6 mas) listed in Table 1 are around integer fractions of the longest excited mode (~1/3, 1/6 and 1/15 of ~100 mas). This indicates that they could be triggered in the jet as harmonics of the fundamental frequency and suggests that a single triggering mechanism (e.g., jet base precession) could be responsible for the whole set of observed oscillation patterns.

[4] The instability wave amplitude is expected to grow with distance, but this leaves the wavelengths unaffected so, assuming that the growth lengths are long enough, this represents an acceptable assumption. Otherwise, the growth should be included to improve the quality of the fits.

Table 1. Results of the fit to the jet ridgeline obtained from the 1.6 GHz image shown in Fig. 1.

Mode	λ [mas]	a [mas]	ψ [°]
1	102 ± 6	2.9 ± 0.2	15 ± 8
2	35 ± 5	0.21 ± 0.03	195 ± 50
3	16.5 ± 1.5	0.55 ± 0.16	−105 ± 30
4	6.6 ± 0.2	0.30 ± 0.05	146 ± 11

Notes. The fits are shown in Fig. 3. These data are adapted from Vega García (2018) and Vega García et al. (2019).

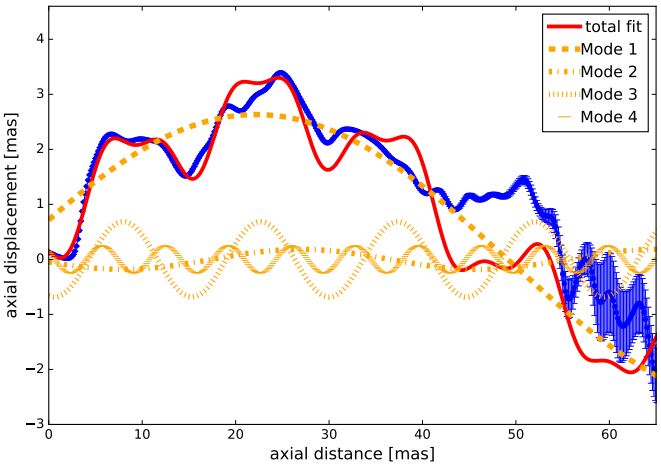

Fig. 3. Fits by oscillatory modes to the jet ridgeline image of one of the Global VLBI images of S5 0836+710 at 1.6 GHz observed on 24 October, 2013. The red line represents the total, multimode fit and the blue lines represent contributions from the individual oscillatory modes as described in the legend. These data are reproduced from Vega García (2018).

3. Stability analysis

The simplest way to explain the observed combination of the oscillations is to assume that all the observed modes grow around the frequencies that correspond to the maximum growth rates for each mode (minimum growth lengths). An initial derivation of the jet parameters can be done using the approximation to the solution of the stability problem given by Hardee (2000). This approximation assumes that the jet is separated from the ambient medium by a contact discontinuity and that the jet Mach number is ≫1. The parameters derived using this approach also depend on an a priori identification of the modes and on the wave speed taken of the mode propagation. The basic jet parameters are then derived from the following equations. The jet Mach number is

$$M_{\rm j} = \frac{\lambda^*(1-\beta_w\cos\theta_{\rm j})}{8R_{\rm j}\gamma_{\rm j}(1-\beta_w/\beta_{\rm j})\sin\theta_{\rm j}}\,, \tag{2}$$

where $\lambda^* = \lambda_i(n_i + 2m_{b_i} + \frac{1}{2})$ is the characteristic wavelength (Lobanov & Zensus 2001), λ_i are the observed (projected) wavelengths and n_i is the azimuthal wavenumber, and m_{b_i} indicates the order of the mode (0 for the surface mode and m_{b_i} for the m_{b_i}-th body mode). The jet-to-ambient medium density ratio is

$$\eta = \frac{M_{\rm j}^2}{M_{\rm x}^2}, \tag{3}$$

where the external jet Mach number, M_x, and the intrinsic jet pattern speeds are calculated with

$$M_x = \frac{\lambda^* \beta_j (1 - \beta_w \cos\theta_j)}{8 R_j \beta_w \sin\theta_j}, \tag{4}$$

$$\beta_w = \frac{\beta_{w,app}}{\sin\theta_j + \beta_{w,app}\cos\theta_j}, \tag{5}$$

and

$$\beta_j = \frac{\beta_{app}}{\sin\theta_j + \beta_{app}\cos\theta_j}, \tag{6}$$

where R_j is the jet radius at the jet base, θ_j is the viewing angle, β_{app} is the apparent speed, and $\beta_{w,app}$ is the apparent pattern speed.

In these expressions, β_w is also difficult to determine, and it has to be taken into account that each developing mode may have a different wave speed. With all these caveats, using the values given in Otterbein et al. (1998), $\theta_j = 3°$ and a bulk Lorentz factor $\gamma_j = 12$, Lobanov et al. (1998) derived a jet classical Mach number of $M_j = 6$ and a jet-to-ambient medium density ratio of $\eta = 0.04$. The three longest wavelengths have been identified as corresponding to the surface, first body, and second body modes, respectively (Vega García 2018). This identification results in $M_j = 12 \pm 3$ and $\eta = 0.33 \pm 0.08$. Differences may be attributed to the different approaches or to the difficulties in the measurement of β_w.

In order to overcome these problems and provide a self-consistent framework for jet modeling, we propose an independent method to derive estimates of the jet parameters from the direct solutions of the stability equation. Taking into account that the presence of a shear layer surrounding the jet in S5 0836+710 has been suggested in earlier works (Perucho & Lobanov 2007, 2011), we solve the differential equation of the linearized stability problem of two flows in pressure equilibrium and relative velocity, for relativistic, sheared jets in cylindrical coordinates (see, e.g., Birkinshaw 1984, 1991):

$$\begin{aligned} 0 = {} & \frac{d^2 p_1(r)}{dr^2} + \\ & \frac{dp_1(r)}{dr}\left\{\frac{1}{r} + \frac{2\gamma_{0,j}(r)^2 \frac{dv_{0,z}(r)}{dr}\left(k - \frac{\omega v_{0,z}(r)}{c^2}\right)}{w - k v_{0,z}(r)} - \frac{\frac{d\rho_0(r)}{dr}}{\rho_0 + \frac{p_0}{c^2}}\right\} + \\ & p_1(r)\left\{\gamma_{0,j}(r)^2\left[\frac{\rho_0(r)(\omega - k v_{0,z}(r))^2}{\Gamma p_0} - \left(k - \frac{\omega v_{0,z}(r)}{c^2}\right)^2\right] - \frac{n^2}{r^2}\right\}, \end{aligned} \tag{7}$$

where r and z are the radial and axial coordinates, k and n are the axial and azimuthal components of the wavenumber, respectively, ω is the frequency, Γ is the adiabatic index, p is the pressure, and subscripts 0 and 1 refer to unperturbed and perturbed variables, respectively. The perturbations are assumed to be proportional to $g(r)\exp(i(k_z z - \omega t))$, where $g(r)$ describes the radial structure of the wave. As in previous works using the same approach (Perucho et al. 2007; Perucho & Lobanov 2007), the shear layer that we consider is described by the variable $a(r)$, corresponding to the velocity or rest-mass density

$$a(r) = a_\infty + (a_0 - a_\infty)/\cosh r^m, \tag{8}$$

where a_0 is the value of the parameter at $r = 0$, a_∞ its value when $r \to \infty$, and m defines the steepness of the layer. This has been shown to converge to the vortex-sheet solution for large enough values of m (Perucho et al. 2005).

We assume an ideal gas equation of state with adiabatic index $\Gamma = 4/3$ to describe both the jet and ambient medium. We take a relativistic hydrodynamics approach, that is, we implicitly assume that the magnetic field is dynamically negligible at the studied scales. Finally, we impose the following boundary conditions:

i. non-incoming waves from infinity (Sommerfeld condition), and
ii. symmetry or antisymmetry of the perturbation and its first derivative on the jet axis.

Then, we obtain the solutions to the differential equation using the shooting method (see Perucho et al. 2005, 2007, for details), which provides us with values for k and ω that satisfy Eq. (7). We used the spatial approach to do this, that is, we assume that the unstable modes grow in distance, because we study how the perturbations grow downstream along the jet. This approach thus uses real frequencies and complex wave numbers. The real part of the wave number describes the wavelength of the perturbation, λ_{int}, and the imaginary part describes the growth length, λ_e:

$$\lambda_{int} = \frac{2\pi}{Re(k)}, \tag{9}$$

$$\lambda_e = -\frac{1}{\mathrm{Im}(k)}. \tag{10}$$

We have solved the equation using a range of shear layer widths, and we have used different values of the Lorentz factor and have swept several orders of magnitude in jet-to-ambient medium density ratios and specific internal energy for each shearing width (see Appendix A for the complete set of solutions obtained). In the calculations, we use units of $\rho_a = 1$, $c = 1$, and $R_j = 1$ (jet radius). Therefore, the jet density in the equations, ρ, represents the density ratio, η, between the jet and the ambient medium.

Specifically, in our parameter space, η ranges from 10^{-5} to 10^{-1}, the jet specific internal energies, ε_j take values from $0.001\,c^2$ to c^2, that is, the calculations include both cold and hot jets, and the shear layer widths range from a narrow layer, as given by $m = 16$ or $m = 12$ ($\leq$10% of the jet radius), to broader ones with $m = 8$ and $m = 4$ ($\simeq$20% of the jet radius). Finally, we considered Lorentz factors from 5 to 17, including $\gamma_j = 12$ as derived from VLBI observations at 8 GHz (Otterbein et al. 1998), $\gamma_j = 17$ from VLBI observations at 15 GHz (Lister et al. 2013), and $\gamma_j = 5$ to study the option of a slower layer of plasma surrounding a fast inner spine.

As a result of the calculations, we obtain a set of physical parameters that provide the best fit to the observed wavelengths, and we can use them to derive an approximation of the Mach number of the flow, using the classical Mach number definition, $M = v_j/c_{sj}$, where the jet sound speed, c_{sj}, can be calculated as

$$c_{sj}^2 = \frac{\Gamma p}{\rho h} = \frac{\Gamma(\Gamma - 1)\varepsilon_j}{1 + \Gamma\varepsilon_j}, \tag{11}$$

where $h = (1 + \Gamma\varepsilon)$ is the specific enthalpy.

In the lower panels of Fig. 4, we indicate the maxima of the imaginary part of the wave number (or minimum growth lengths) for each mode. This allows us to derive the intrinsic wavelength of the modes by looking for the maximum in values of the wave number in the upper plots. Since the curves do not have sharp maxima, but plateau-like maxima, we consider the points where the maximum value of the imaginary part for each mode of the wave number is reduced by 5% as lower and upper bounds. In order to compare our results with

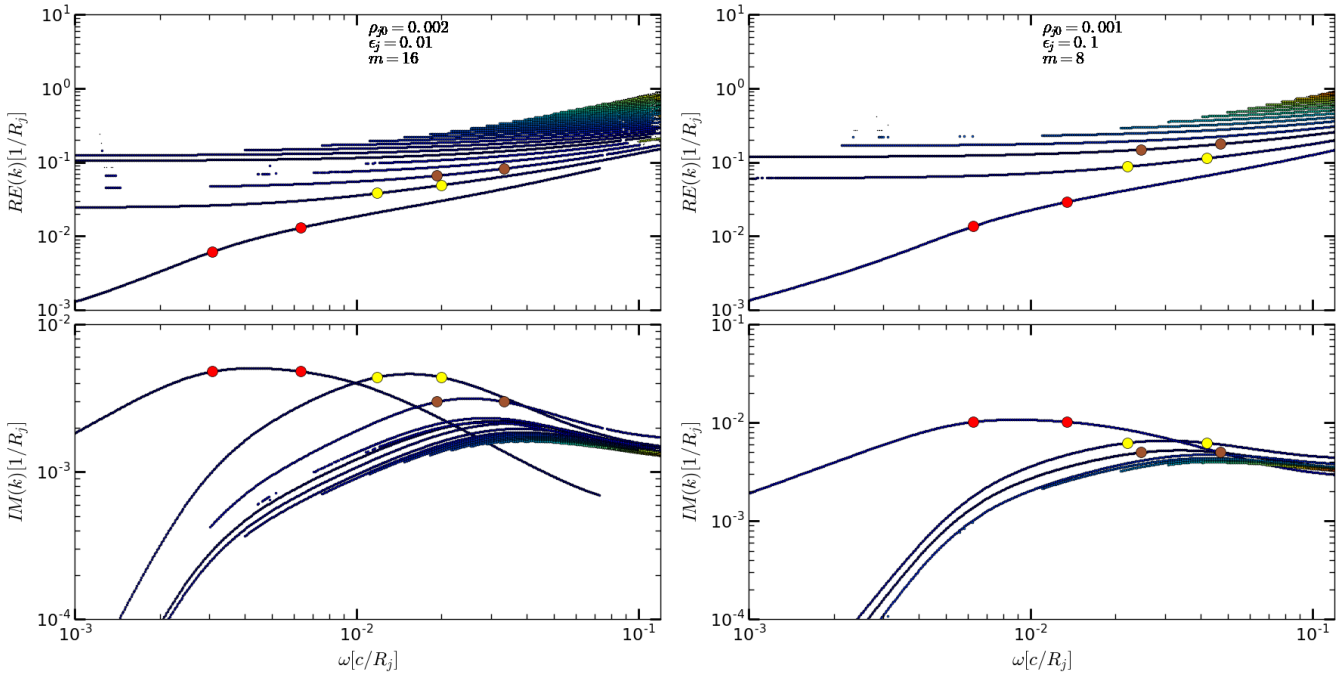

Fig. 4. Example solutions of the stability equation for helical modes applied to the jet of S5 0836+710. *Upper panel*: wave number and *lower panel*: growth length as function of the frequency. The colored dots represent the values for which the maximum value of the imaginary part of the wave number is reduced by 5%, that is, the interval where the growth length is minimized. The red dots correspond to the helical surface mode, the yellow dots to the first body mode, and the brown ones to the second body mode. *Left panel*: solutions for a shear layer of $m = 16$, jet internal energy of 0.01, and jet density of 0.002. *Right panel*: solutions for a shear layer of $m = 8$, jet internal energy of 0.01, and jet density of 0.001.

the fitted structures from observations, we convert the distance unit used in the calculations (jet radius, R_j) into milliarcseconds, using the jet radius at the jet base derived from observations ($1\,R_j = 2$ mas, Vega García 2018). In this respect, we note that the stability problem is solved for an infinite, cylindrical jet, but jet expansion introduces an increase of the mode peak wavelengths (e.g., Hardee 1982, 1984, 1986) so our assumption represents a source of uncertainty. However, the jet opening angle for the jet in S5 0836+710 is very small (<1°, see Perucho et al. 2012a), and we can regard our solutions as a plausible approach to the jet parameters.

The corresponding observed wavelength can be then derived from the calculated intrinsic wavelength, using the viewing angle, θ, and the intrinsic wave speed, β_ω:

$$\lambda_{\rm obs} = \lambda_{\rm int} \frac{\sin\theta}{1 - \beta_\omega \cos\theta}. \tag{12}$$

The intrinsic wave speed has been estimated using the values of the complex k and real ω from the calculations using

$$\beta_\omega = \frac{\omega}{k} \sim Re\left(\frac{\omega}{k}\right), \tag{13}$$

where $Re(k) \gg \mathrm{Im}(k)$.

4. Results: jet parameters

The values of the peak wavelengths that result from the solution of Eq. (7) for each set of parameters and the Mach numbers derived from them can be found in Tables A.1–A.6. In order to illustrate how the predicted observed wavelengths change with the shear layer width and the jet parameters, we have plotted in Fig. 5 the wavelengths obtained for the relevant modes as a function of rest-mass density ratio for each value of the shear layer and jet internal energy. This figure only shows the best result (given by the most probable set of jet parameters) and a further three interesting examples. Additional figures can be found in Appendix A. In the plots, the horizontal lines and shades indicate the observed wavelengths and their formal errors. Each "family" of three points in the y direction represents the wavelengths at the maxima in growth rate of the fundamental, first, and second body modes for each different model (defined by the given set of physical parameters). The most likely model is thus the one for which the points lie closer to the observed wavelengths (horizontal lines) within the error given by the shaded areas.

If we first compare the effect of the shear layer on the simulated observed wavelengths, we can see that the broader the shear layer, the larger the separation between the peaks of the fundamental mode and the first body mode, while the narrower the shear layer, the smaller the separation between these modes. This ratio excludes wide shear layers extending more than $1\,R_j$ (e.g., $m \geq 4$). The ratio between the observed wavelengths indicates a narrower shear layer width, $m = 16$ (with an extension of $0.1{-}0.2\,R_j$), as the most likely scenario. Regarding the effect of the physical parameters of the jet, an increase of the density ratio reduces the peak wavelengths, since it causes an increase of the specific internal energy, whereas increasing the Lorentz factor increases those wavelengths. These solid trends have allowed us to exclude wide regions of the parameter space.

The dispersion between the observed wavelengths and the calculated ones can be used to determine which of the parameter sets best recovers the observed values given in Sect. 2. The two models with lower dispersions are the ones with $\eta = 2\times10^{-3}$ and $\varepsilon_j = 0.01c^2$, and $\eta = 10^{-3}$ and $\varepsilon_j = 0.01c^2$. Both cases would

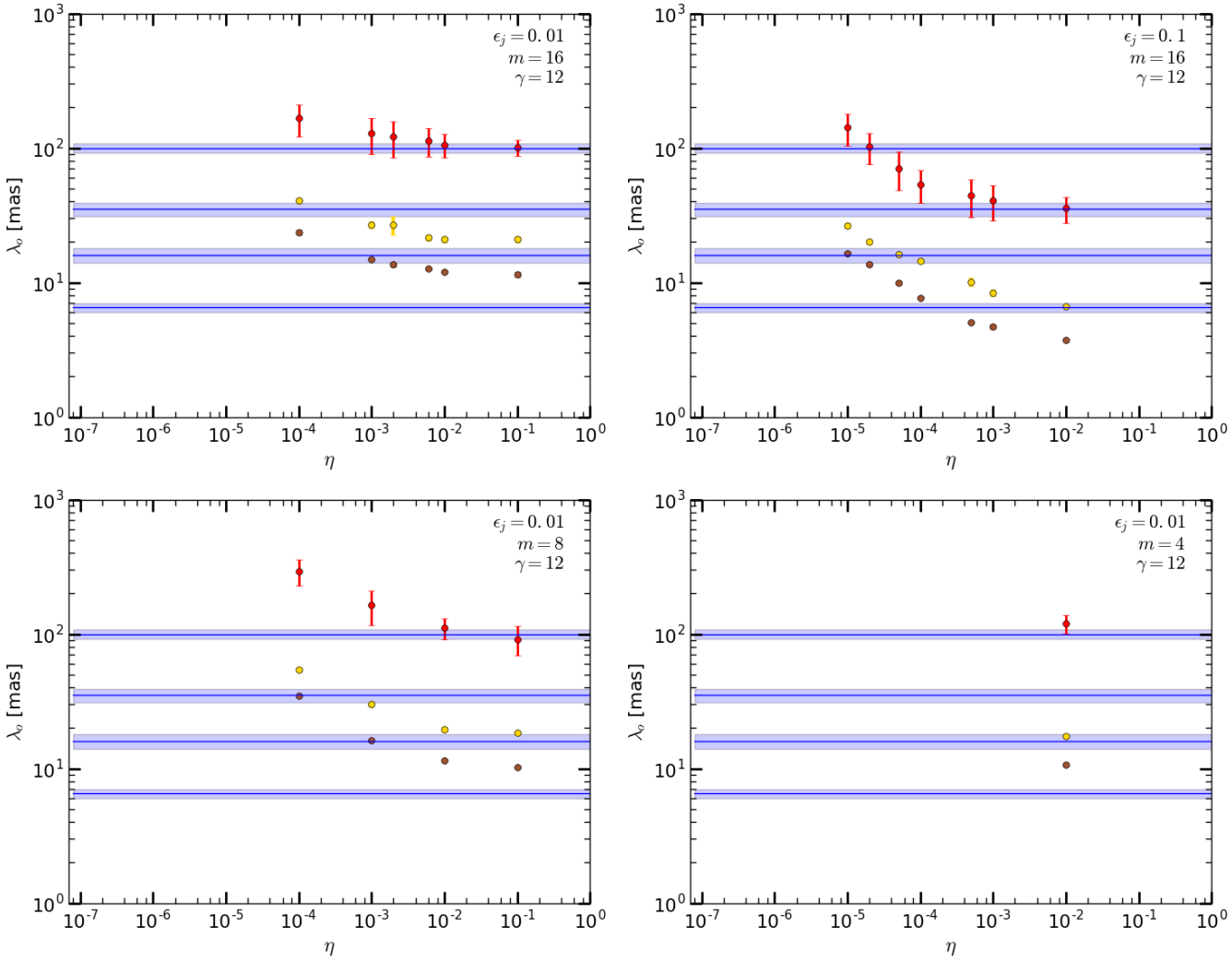

Fig. 5. Observed wavelengths and their errors (blue lines and shades) compared to the wavelengths of different instability modes (symbols) obtained from the linear stability analysis. The color scheme used for representing the calculated wavelengths is the same as the one used in Fig. 4. The x-axis represents the density ratio and the y-axis the corresponding observed wavelength. *Upper left panel*: results for a shear layer of steepness $m = 16$ and jet internal energy of 0.01. *Upper right panel*: results for a shear layer of steepness $m = 16$ and jet internal energy of 0.1. *Lower left panel*: results for a shear layer of steepness $m = 8$ and jet internal energy of 0.01. *Lower right panel*: results for a shear layer of steepness $m = 4$ and jet internal energy of 0.01.

correspond to a Mach number of $M \sim 12$. This value coincides with the value obtained independently from the approximations used in previous works (see Sect. 3). The specific internal energy of the jet is clearly lower than one (c^2), which places the jet in the cold regime, possibly dominated by the kinetic energy.

We have also computed the solutions for different jet Lorentz factor values, $\gamma_j = 5$ and $\gamma_j = 17$, for the best fitting values of ε_j and η. We found that the case of $\gamma_j = 17$ results in peak wavelengths that are compatible with the observed wavelengths for each of the helical modes proposed (surface, and first and second body modes), whereas the $\gamma_j = 5$ models systematically result in lower peak wavelengths for each of the modes. Comparing the results given by Lorentz factors 12 and 17, we see that although both models could still be compatible, the dispersion between the calculated wavelengths and the observed ones is lower for the Lorentz factor of 12 (see Tables A.1–A.6). It is noteworthy that the parameter sets that give the lowest dispersion for Lorentz factor 17 include options with larger values of ε_j ($0.01–0.1\,c^2$) and smaller η ($10^{-5}–10^{-4}$). Finally, although we found relatively small dispersion values for parameter sets with $\gamma = 12$ and higher values of ε_j ($1–10\,c^2$), the density ratios are extremely small ($10^{-7}–10^{-6}$), and still the dispersion is larger than for the aforementioned parameter sets.

Our results thus allow us to confirm that the Lorentz factor of the jet at the scales revealed by the 1.6 GHz jet is probably in the range 12–17, in agreement with the estimated value by Otterbein et al. (1998) from jet kinematics at 8 GHz and that derived by Lister et al. (2013) from 15 GHz observations. For these values of the Lorentz factor, we find that the jet is remarkably underdense with respect to its environment ($\eta \sim 10^{-5}–10^{-3}$) and relatively cold ($\varepsilon_j \sim 0.01–0.1\,c^2$). This results in a relativistic jet Mach number, $\mathcal{M}_j \simeq \gamma_j M_j$, range of 60–144.

5. Discussion and conclusions

Our calculations include the following basic assumptions: (1) infinite cylindrical jet, and (2) dynamically negligible magnetic field. Because we model the observed jet structures over >100 mas in length, representing linear scales of ~10 kpc, and

recalling that the jet flow may change considerably along this distance, we have to discuss the validity of our results as estimates of mean jet parameters. On the one hand, taking into account that the analysis pictures a cold and fast jet, and that our estimate of the Lorentz factor coincides with that derived by Otterbein et al. (1998) from jet kinematics at 8 GHz, we can infer that any kind of Bernoulli acceleration (internal energy conversion into kinetic energy) must have taken place upstream and that no further acceleration takes place along the observed jet at 1.6 GHz. This argumentation consolidates the value of the Lorentz factor of $\gamma \simeq 12$ for the whole VLBI jet in S5 0836+710. The high degree of collimation of this jet also allows us to take the derived values of the specific internal energy, and density ratio can be regarded as an order of magnitude estimate because the limited jet expansion will lead to a relatively small drop in both parameters. As far as the dynamical role of the magnetic field, magnetic acceleration models (e.g., Vlahakis & Königl 2004; Komissarov et al. 2012), and observational (e.g., Homan et al. 2015; Boccardi et al. 2016; Mertens et al. 2016) results seem to point towards magnetic acceleration taking place at the inner tens of parsecs, at most, from injection, so a magnetically dominated jet is not expected at kiloparsec scales, like those involved in the VLBI jet of S5 0836+710. In addition, our results tend to favor a kinetically dominated jet, with relatively low internal energy and high Lorentz factor (as expected for particle dominated flows, Martí et al. 2016). This can be taken as a self-consistency test for our initial hypothesis of the observed structures being generated by KH instability modes. The similarity between the inferred Lorentz factor and that given by previous kinematic studies (Otterbein et al. 1998; Lister et al. 2013) validates our approach and encourages us to propose it as a possible way to derive jet parameters in other cases, for the range of distances in which the assumptions are fulfilled. Namely, small jet opening angles and linear-growth regime of the modes (implying relatively small changes in the wave amplitude).

Because the calculations assume that the jet parameters are constant in the axial direction, we have to consider the parameters derived as mean values along the observed VLBI jet. Further work should include genetic or machine learning algorithms in the application of this method to the determination of jet parameters.

The values derived for the jet Lorentz factor and Mach number result in a relativistic Mach number of $\mathcal{M}_j \sim 60-144$ (c.f. the classical Mach number $M_j = 5-12$). The jet would thus be well within the stable region of the relativistic jet stability plane shown in Perucho et al. (2005, Fig. 21 in that paper) with very small growth-rate unstable modes (which validates the modeling assumption of constant wave amplitudes in Eq. (1)) and prone to the development of stabilizing, short-wavelength resonant modes (Perucho et al. 2007, 2010). This is probably in contradiction to the conclusion of Perucho et al. (2012b), where the authors claim that the jet may be disrupted by the growth of instabilities, giving rise to the decollimated structure observed with MERLIN at arcsecond scales. This structure was interpreted by the authors as a sign of jet disruption, but this work and recent observational results (Kappes et al., in prep.) may indicate that the arcsecond emission region related to this source may reveal the interaction site of the jet with the intracluster medium.

The results obtained in this work can be summarized as follows:

- We have used the results from previous studies of the S5 0836+710 jet structure that have modeled its ridgeline at 1.6 GHz, which covers up to ≃130 mas, by fitting transverse brightness profiles with a single Gaussian component.
- The ridgeline shows the presence of several oscillatory terms, which have been reported in several different works (Lobanov et al. 1998, 2006; Perucho et al. 2012a). All those previous works give similar values for the wavelengths of the most prominent oscillations, using different arrays and epochs of observation.
- We assume that these oscillations correspond to KH instability modes developing in the flow, and propose a method to derive the physical parameters of the jet. The method requires solving numerically the stability problem for a wide range of values of the relevant jet parameters and comparing the wavelengths at the maximum growth rates for the identified modes plus their ratios with the observed structures.
- This method does not need any a priori known parameters, but only the solving of the linear stability problem for a wide region of the parameter space. From this approach, we find a jet Lorentz factor in the range $\gamma \simeq 12-17$, in coincidence with kinematical studies (Otterbein et al. 1998; Lister et al. 2013), and, within that range, the jet-to-ambient medium density ratio is found to be $\eta \sim 10^{-5}-10^{-3}$, and the jet specific internal energy is $\varepsilon \sim 10^{-2}-10^{-1}\, c^2$, resulting in a jet classical Mach number of $M \sim 5-12$. We also found that the observed radio jet is surrounded by a thin shear layer, with a width $\simeq 10$ % of the jet radius. The value derived for the specific internal energy and the Lorentz factor point towards a kinetically dominated jet.

Acknowledgements. L.V.G is a member of the International Max Planck Research School (IMPRS) for Astronomy and Astrophysics at the Universities of Bonn and Cologne. This research is based on observations correlated at the Bonn Correlator, jointly operated by the Max Planck Institute for Radio Astronomy (MPIfR), and the Federal Agency for Cartography and Geodesy (BKG). The European VLBI Network is a joint facility of European, Chinese, South African, and other radio astronomy institutes funded by their national research councils. The National Radio Astronomy Observatory is a facility of the National Science Foundation operated under cooperative agreement by Associated Universities, Inc. Thanks to Phillip Edward, Alan Roy, and Víctor M. Patiño Álvarez for the useful comments about the paper. We thank the anonymous referee for useful comments that improved the manuscript. MP has been supported by the Spanish Ministerio de Economía y Competitividad (grants AYA2015-66899-C2-1-P and AYA2016-77237-C3-3-P) and the Generalitat Valenciana (grant PROMETEOII/2014/069). The authors want to thank P.E. Hardee for his inspiring work.

References

Bach, U., Villata, M., Raiteri, C. M., et al. 2006, A&A, 456, 105
Birkinshaw, M. 1984, MNRAS, 208, 887
Birkinshaw, M. 1991, MNRAS, 252, 505
Blandford, R. D., & Znajek, R. L. 1977, MNRAS, 179, 433
Boccardi, B., Krichbaum, T. P., Bach, U., et al. 2016, A&A, 585, A33
Cohen, M. H., Meier, D. L., Arshakian, T. G., et al. 2015, ApJ, 803, 3
Hardee, P. E. 1982, ApJ, 257, 509
Hardee, P. E. 1984, ApJ, 287, 523
Hardee, P. E. 1986, ApJ, 303, 111
Hardee, P. E. 2000, ApJ, 533, 176
Hirabayashi, H., Hirosawa, H., Kobayashi, H., et al. 2000, PASJ, 52, 955
Homan, D. C., Lister, M. L., Kovalev, Y. Y., et al. 2015, ApJ, 798, 134
Hummel, C. A., Muxlow, T. W. B., Krichbaum, T. P., et al. 1992, A&A, 266, 93
Komissarov, S. 2012, in Central Engines: Acceleration, Collimation and Confinement of Jets, eds. M. Boettcher, D. E. Harris, & H. Krawczynski, 81
Krichbaum, T. P., Hummel, C. A., Quirrenbach, A., et al. 1990, A&A, 230, 271
Lister, M. L., Kellermann, K. I., Vermeulen, R. C., et al. 2003, ApJ, 584, 135
Lister, M. L., Aller, M. F., Aller, H. D., et al. 2013, AJ, 146, 120
Lobanov, A. P., & Roland, J. 2005, A&A, 431, 831
Lobanov, A. P., & Zensus, J. A. 2001, Science, 294, 128
Lobanov, A. P., Krichbaum, T. P., Witzel, A., et al. 1998, A&A, 340, L60

Lobanov, A. P., Krichbaum, T. P., Witzel, A., & Zensus, J. A. 2006, PASJ, 58, 253
Martí, J. M., Perucho, M., & Gómez, J. L. 2016, ApJ, 831, 163
McKinney, J. C., & Blandford, R. D. 2009, MNRAS, 394, L126
McNamara, B. R., & Nulsen, P. E. J. 2012, New J. Phys., 14, 055023
Mertens, F., Lobanov, A. P., Walker, R. C., & Hardee, P. E. 2016, A&A, 595, A54
Mignone, A., Rossi, P., Bodo, G., Ferrari, A., & Massaglia, S. 2010, MNRAS, 402, 7
Mizuno, Y., Hardee, P., & Nishikawa, K.-I. 2007, ApJ, 662, 835
Mizuno, Y., Lyubarsky, Y., Nishikawa, K.-I., & Hardee, P. E. 2009, ApJ, 700, 684
Mizuno, Y., Hardee, P. E., & Nishikawa, K.-I. 2011, ApJ, 734, 19
Osmer, P. S., Porter, A. C., & Green, R. F. 1994, ApJ, 436, 678
Otterbein, K., Krichbaum, T. P., & Kraus, A. 1998, ASP Conf. Ser., 144, 73
Perucho, M., & Lobanov, A. P. 2007, A&A, 469, L23
Perucho, M., & Lobanov, A. P. 2011, A&A, 533, C2
Perucho, M., Lobanov, A. P., & Martí, J. M. 2005, Mem. Soc. Astron. It., 76, 110
Perucho, M., Hanasz, M., Martí, J.-M., & Miralles, J.-A. 2007, Phys. Rev. E, 75, 056312
Perucho, M., Martí, J. M., Cela, J. M., et al. 2010, A&A, 519, A41
Perucho, M., Kovalev, Y. Y., Lobanov, A. P., Hardee, P. E., & Agudo, I. 2012a, ApJ, 749, 55
Perucho, M., Martí-Vidal, I., Lobanov, A. P., & Hardee, P. E. 2012b, A&A, 545, A65
Planck Collaboration XIII. 2016, A&A, 594, A13
Savolainen, T., Wiik, K., Valtaoja, E., & Tornikoski, M. 2006, A&A, 446, 71
Stirling, A. M., Cawthorne, T. V., Stevens, J. A., et al. 2003, MNRAS, 341, 405
Vega García, L. 2018, Space VLBI studies of Internal Structure and Physical Processes in Extragalactic Relativistic Jets. PhD Thesis, Universität zu Köln
Vega-García, L., Perucho, M., & Lobanov, A. P. 2019, A&A, submitted, [arXiv:1904.02030]
Vlahakis, N., & Königl, A. 2004, ApJ, 605, 656

Appendix A: Results of the calculations for the stability studies

Here we present the table with all the values of the simulated observed wavelengths and the estimated Mach number values for all the calculations presented throughout the paper. We also present the remaining plots of $\lambda_{\rm obs}$ as a function of the density ratio obtained from this analysis (Sect. 4).

Table A.1. Solutions of the dispersion relation for $m = 16$ and $\gamma = 12$.

Mode	m	$\varepsilon_{\rm j}$	η	$M_{\rm j}$	ω [$c/R_{\rm j}$]	$Re(k)$ [$1/R_{\rm j}$]	λ [mas]	Dispersion
H_s	16	10	10^{-7}	1.55	0.0019–0.0052	0.0054–0.0117	96.69–167.61	
H_{b_1}	16	10	10^{-7}	1.55	0.0053–0.014	0.0310–0.0380	23.82–25.59	0.135
H_{b_2}	16	10	10^{-7}	1.55	0.0070–0.0120	0.0520–0.0590	14.00–14.62	
H_s	16	1	10^{-6}	1.94	0.0018–0.0050	0.0052–0.0110	103.97–171.92	
H_{b_1}	16	1	10^{-6}	1.94	0.0050–0.010	0.0310–0.0380	23.48–25.29	0.171
H_{b_2}	16	1	10^{-6}	1.94	0.0060–0.0125	0.0500–0.0590	14.15–14.96	
H_s	16	1	10^{-5}	1.94	0.0055–0.0150	0.0160–0.0340	32.91–55.65	
H_{b_1}	16	1	10^{-5}	1.94	0.0150–0.0280	0.0900–0.1100	8.02–8.77	0.774
H_{b_2}	16	1	10^{-5}	1.94	0.0205–0.0400	0.1300–0.1600	5.48–6.01	
H_s	16	1	10^{-4}	1.94	0.012–0.034	0.033–0.076	14.7–26.7	
H_{b_1}	16	1	10^{-4}	1.94	0.050–0.090	0.180–0.230	4.69–5.05	1.207
H_{b_2}	16	1	10^{-4}	1.94	0.050–0.090	0.310–0.365	2.39–2.53	
H_s	16	1	0.001	1.94	0.023–0.056	0.046–0.105	12.23–21.57	
H_{b_1}	16	1	0.001	1.94	0.086–0.151	0.310–0.400	2.63–2.93	1.358
H_{b_2}	16	1	0.001	1.94	0.127–0.221	0.520–0.630	1.61–1.67	
H_s	16	0.1	10^{-5}	4.21	0.0018–0.0050	0.0050–0.0110	103.97–180.10	
H_{b_1}	16	0.1	10^{-5}	4.21	0.0050–0.010	0.0290–0.0360	25.28–27.40	0.187
H_{b_2}	16	0.1	10^{-5}	4.21	0.0060–0.0110	0.0450–0.0520	16.05–16.87	
H_s	16	0.1	2×10^{-5}	4.21	0.0025–0.0067	0.0070–0.0150	75.20–128.62	
H_{b_1}	16	0.1	2×10^{-5}	4.21	0.0064–0.0120	0.0380–0.0460	19.34–20.81	0.183
H_{b_2}	16	0.1	2×10^{-5}	4.21	0.010–0.0220	0.0570–0.0710	13.42–14.00	
H_s	16	0.1	5×10^{-5}	4.21	0.0040–0.010	0.010–0.0230	48.22–93.20	
H_{b_1}	16	0.1	5×10^{-5}	4.21	0.010–0.0190	0.0500–0.0600	16.04–16.45	0.332
H_{b_2}	16	0.1	5×10^{-5}	4.21	0.0130–0.0260	0.0770–0.0940	9.67–10.28	
H_s	16	0.1	10^{-4}	4.21	0.0045–0.0126	0.0129–0.0286	38.88–68.18	
H_{b_1}	16	0.1	10^{-4}	4.21	0.0160–0.0330	0.0600–0.0800	13.98–14.94	0.487
H_{b_2}	16	0.1	10^{-4}	4.21	0.0170–0.0325	0.1–0.1200	7.51–7.92	
H_s	16	0.1	5×10^{-4}	4.21	0.0060–0.0160	0.0150–0.0360	30.45–58.02	
H_{b_1}	16	0.1	5×10^{-4}	4.21	0.0300–0.0500	0.0900–0.1200	9.35–10.90	0.755
H_{b_2}	16	0.1	5×10^{-4}	4.21	0.0300–0.0600	0.1600–0.1900	5.06–5.06	
H_s	16	0.1	0.001	4.21	0.007–0.017	0.017–0.038	28.71–53.06	
H_{b_1}	16	0.1	0.001	4.21	0.033–0.057	0.107–0.140	7.88–8.84	0.972
H_{b_2}	16	0.1	0.001	4.21	0.050–0.090	0.186–0.236	4.50–4.84	
H_s	16	0.1	0.01	4.21	0.019–0.035	0.030–0.056	27.79–43.23	
H_{b_1}	16	0.1	0.01	4.21	0.063–0.110	0.160–0.210	6.56–6.77	0.972
H_{b_2}	16	0.1	0.01	4.21	0.080–0.140	0.250–0.320	3.65–3.87	
H_s	16	0.01	10^{-4}	12.53	0.0015–0.0041	0.0042–0.0092	121.71–211.18	
H_{b_1}	16	0.01	10^{-4}	12.53	0.0050–0.010	0.0200–0.0260	39.00–41.94	0.499
H_{b_2}	16	0.01	10^{-4}	12.53	0.0054–0.010	0.0320–0.0390	22.68–24.73	
H_s	16	0.01	10^{-3}	12.53	0.0024–0.0055	0.0054–0.0122	89.69–166.25	
H_{b_1}	16	0.01	10^{-3}	12.53	0.0110–0.0190	0.0340–0.0450	25.14–28.41	0.096
H_{b_2}	16	0.01	10^{-3}	12.53	0.0160–0.0310	0.0600–0.0760	14.61–14.95	
H_s	16	0.01	2×10^{-3}	12.53	0.0030–0.0060	0.0060–0.0130	85.19–157.74	
H_{b_1}	16	0.01	2×10^{-3}	12.53	0.0120–0.0200	0.0330–0.0490	22.55–31.01	0.075
H_{b_2}	16	0.01	2×10^{-3}	12.53	0.0190–0.0330	0.0660–0.0830	13.14–13.99	
H_s	16	0.01	6×10^{-3}	12.53	0.0045–0.0084	0.0078–0.0152	85.60–140.39	
H_{b_1}	16	0.01	6×10^{-3}	12.53	0.0150–0.0250	0.0440–0.0570	20.47–22.59	0.155
H_{b_2}	16	0.01	6×10^{-3}	12.53	0.0210–0.0360	0.0720–0.0890	12.40–12.89	
H_s	16	0.01	0.01	12.53	0.006–0.011	0.01–0.018	84.37–126.43	
H_{b_1}	16	0.01	0.01	12.53	0.019–0.033	0.049–0.066	19.86–21.85	0.174
H_{b_2}	16	0.01	0.01	12.53	0.025–0.045	0.079–0.100	11.95–12.18	
H_s	16	0.01	0.1	12.53	0.015–0.022	0.020–0.029	87.23–114.63	
H_{b_1}	16	0.01	0.1	12.53	0.047–0.078	0.077–0.111	19.85–21.84	0.183
H_{b_2}	16	0.01	0.1	12.53	0.070–0.120	0.125–0.180	10.94–11.94	
H_s	16	0.001	0.1	39.36	0.005–0.007	0.006–0.009	302.69–520.51	
H_{b_1}	16	0.001	0.1	39.36	0.016–0.021	0.025–0.031	65.50–72.76	9.963
H_{b_2}	16	0.001	0.1	39.36	0.027–0.035	0.045–0.051	41.00–36.48	

Table A.2. Solutions of the dispersion relation for $m = 8$ and $\gamma = 12$.

Mode	m	ε_j	η	M_j	$\omega\ [c/R_j]$	$Re(k)\ [1/R_j]$	λ [mas]	Dispersion
H_s	8	1	10^{-6}	1.94	0.0010–0.0020	0.0030–0.0052	195.02–296.18	
H_{b_1}	8	1	10^{-6}	1.94	0.0030–0.0044	0.0160–0.0190	45.03–50.57	2.166
H_{b_2}	8	1	10^{-6}	1.94	0.0035–0.0047	0.0280–0.0300	26.01–26.86	
H_s	8	1	10^{-5}	1.94	0.0024–0.0071	0.0065–0.0164	66.41–131.81	
H_{b_1}	8	1	10^{-5}	1.94	0.0080–0.0160	0.0500–0.0620	14.29–15.66	0.384
H_{b_2}	8	1	10^{-5}	1.94	0.010–0.0200	0.0820–0.0970	8.54–9.14	
H_s	8	1	10^{-4}	1.94	0.007–0.019	0.018–0.044	24.59–48.24	
H_{b_1}	8	1	10^{-4}	1.94	0.024–0.047	0.126–0.156	6.03–6.45	0.989
H_{b_2}	8	1	10^{-4}	1.94	0.030–0.060	0.205–0.249	3.48–3.76	
H_s	8	1	0.001	1.94	0.019–0.038	0.038–0.077	15.33–26.25	
H_{b_1}	8	1	0.001	1.94	0.061–0.114	0.265–0.336	2.96–3.22	1.307
H_{b_2}	8	1	0.001	1.94	0.083–0.161	0.445–0.540	1.74–1.82	
H_s	8	0.1	10^{-5}	4.21	0.0010–0.0022	0.0027–0.0052	206.16–335.70	
H_{b_1}	8	0.1	10^{-5}	4.21	0.0026–0.0053	0.0160–0.0200	44.57–49.07	2.956
H_{b_2}	8	0.1	10^{-5}	4.21	0.0032–0.0064	0.0270–0.0320	25.70–27.65	
H_s	8	0.1	10^{-4}	4.21	0.0024–0.0066	0.0060–0.0150	73.34–146.59	
H_{b_1}	8	0.1	10^{-4}	4.21	0.0075–0.0140	0.0440–0.0530	16.86–18.02	0.269
H_{b_2}	8	0.1	10^{-4}	4.21	0.010–0.0210	0.0680–0.0820	10.78–11.35	
H_s	8	0.1	0.001	4.21	0.006–0.013	0.014–0.029	37.84–65.61	
H_{b_1}	8	0.1	0.001	4.21	0.022–0.042	0.090–0.110	9.65–9.66	0.738
H_{b_2}	8	0.1	0.001	4.21	0.025–0.047	0.150–0.180	4.95–5.26	
H_s	8	0.1	0.01	4.21	0.016–0.027	0.028–0.048	28.09–42.24	
H_{b_1}	8	0.1	0.01	4.21	0.044–0.080	0.150–0.190	5.97–6.20	1.003
H_{b_2}	8	0.1	0.01	4.21	0.051–0.091	0.230–0.280	3.48–3.67	
H_s	8	0.01	10^{-4}	12.53	0.0010–0.0021	0.0026–0.0048	227.82–355.68	
H_{b_1}	8	0.01	10^{-4}	12.53	0.0024–0.0045	0.0140–0.0170	52.60–56.70	3.931
H_{b_2}	8	0.01	10^{-4}	12.53	0.0032–0.0068	0.0220–0.0260	34.26–35.00	
H_s	8	0.01	10^{-3}	12.53	0.0020–0.0043	0.0044–0.0095	116.13–210.87	
H_{b_1}	8	0.01	10^{-3}	12.53	0.0070–0.0140	0.0280–0.0364	29.31–31.28	0.404
H_{b_2}	8	0.01	10^{-3}	12.53	0.0080–0.0150	0.0480–0.0565	15.85–16.45	
H_s	8	0.01	0.01	12.53	0.005–0.009	0.009–0.015	90.54–130.82	
H_{b_1}	8	0.01	0.01	12.53	0.014–0.025	0.046–0.060	18.76–20.52	0.208
H_{b_2}	8	0.01	0.01	12.53	0.017–0.030	0.073–0.088	11.33–11.74	
H_s	8	0.01	0.1	12.53	0.012–0.017	0.017–0.026	69.32–114.11	
H_{b_1}	8	0.01	0.1	12.53	0.035–0.056	0.070–0.092	17.98–18.76	0.260
H_{b_2}	8	0.01	0.1	12.53	0.043–0.078	0.106–0.143	10.11–10.44	
H_s	8	0.001	0.1	39.36	0.004–0.005	0.005–0.008	246.47–507.97	
H_{b_1}	8	0.001	0.1	39.36	0.012–0.016	0.023–0.027	59.67–59.69	7.850
H_{b_2}	8	0.001	0.1	39.36	0.023–0.030	0.040–0.050	32.83–38.62	

Table A.3. Solutions of the dispersion relation for $m = 4$ and $\gamma = 12$.

Mode	m	ε_j	η	M_j	$\omega\ [c/R_j]$	$Re(k)\ [1/R_j]$	λ [mas]	Dispersion
H_s	4	1	0.0001	1.94	0.005–0.01	0.015–0.023	47.11–59.81	
H_{b_1}	4	1	0.0001	1.94	0.013–0.028	0.086–0.108	8.22–9.01	0.765
H_{b_2}	4	1	0.0001	1.94	0.016–0.035	0.140–0.170	4.87–5.31	
H_s	4	0.1	0.001	4.21	0.005–0.009	0.01–0.020	55.56–101.93	
H_{b_1}	4	0.1	0.001	4.21	0.013–0.026	0.070–0.090	10.27–11.54	0.606
H_{b_2}	4	0.1	0.001	4.21	0.015–0.033	0.120–0.140	6.15–6.27	
H_s	4	0.01	0.01	12.53	0.004–0.007	0.008–0.013	100.35–138.85	
H_{b_1}	4	0.01	0.01	12.53	0.01–0.019	0.047–0.058	16.86–17.78	0.280
H_{b_2}	4	0.01	0.01	12.53	0.013–0.026	0.073–0.089	10.44–10.97	
H_s	4	0.001	0.1	39.36	0.003–0.004	0.005–0.007	197.60–287.79	
H_{b_1}	4	0.001	0.1	39.36	0.014–0.018	0.027–0.032	43.65–46.53	2.09
H_{b_2}	4	0.001	0.1	39.36	0.014–0.018	0.039–0.041	27.79–25.73	

Table A.4. Solutions of the dispersion relation for $m = 12$ and $\gamma = 12$.

Mode	m	ε_j	η	M_j	$\omega\ [c/R_j]$	$Re(k)\ [1/R_j]$	λ [mas]	Dispersion
H_s	12	0.01	10^{-5}	4.21	0.0012–0.0036	0.0034–0.0083	133.23–257.61	
H_{b_1}	12	0.01	10^{-5}	4.21	0.0039–0.0079	0.0230–0.0290	31.15–34.43	0.912
H_{b_2}	12	0.01	10^{-5}	4.21	0.0045–0.0088	0.0370–0.0430	19.24–20.25	
H_s	12	0.01	6×10^{-5}	4.21	0.0030–0.0080	0.0077–0.0185	59.55–117.70	
H_{b_1}	12	0.01	6×10^{-5}	4.21	0.0080–0.0150	0.0455–0.0547	16.56–17.54	0.280
H_{b_2}	12	0.01	6×10^{-5}	4.21	0.0120–0.0240	0.0700–0.0850	10.78–11.34	
H_s	12	0.1	10^{-4}	4.21	0.0030–0.010	0.0090–0.0230	47.94–93.90	
H_{b_1}	12	0.1	10^{-4}	4.21	0.0110–0.0210	0.0530–0.0650	14.94–15.66	0.376
H_{b_2}	12	0.1	10^{-4}	4.21	0.0140–0.0280	0.0840–0.1020	8.89–9.40	

Table A.5. Solutions of the dispersion relation for $m = 16$ and $\gamma = 5$.

Mode	m	ε_j	η	M_j	$\omega\ [c/R_j]$	$Re(k)\ [1/R_j]$	λ [mas]	Dispersion
H_s	16	0.01	0.001	12.53	0.004–0.010	0.012–0.027	37.26–67.77	
H_{b_1}	16	0.01	0.001	12.53	0.019–0.036	0.062–0.084	13.68–15.38	0.508
H_{b_2}	16	0.01	0.001	12.53	0.014–0.026	0.103–0.118	7.10–7.36	
H_s	16	0.01	0.002	12.53	0.004–0.011	0.012–0.028	35.49–68.72	
H_{b_1}	16	0.01	0.002	12.53	0.021–0.037	0.071–0.094	11.55–13.20	0.590
H_{b_2}	16	0.01	0.002	12.53	0.025–0.054	0.123–0.156	6.45–6.71	
H_s	16	0.1	2×10^{-5}	4.21	0.003–0.008	0.010–0.021	50.50–85.77	
H_{b_1}	16	0.1	2×10^{-5}	4.21	0.008–0.016	0.056–0.068	12.64–13.86	0.467
H_{b_2}	16	0.1	2×10^{-5}	4.21	0.009–0.017	0.088–0.100	7.93–8.32	

Table A.6. Solutions of the dispersion relation for $\gamma = 17$.

Mode	m	ε_j	η	M_j	$\omega\ [c/R_j]$	$Re(k)\ [1/R_j]$	λ [mas]	Dispersion
H_s	25	0.01	0.001	12.55	0.002–0.005	0.005–0.010	116.90–206.14	
H_{b_1}	25	0.01	0.001	12.55	0.009–0.015	0.028–0.036	30.57–34.39	0.380
H_{b_2}	25	0.01	0.001	12.55	0.017–0.026	0.050–0.062	18.50–19.57	
H_s	25	0.01	0.002	12.55	0.003–0.006	0.005–0.011	115.94–195.36	
H_{b_1}	25	0.01	0.002	12.55	0.011–0.018	0.031–0.040	29.61–32.61	0.310
H_{b_2}	25	0.01	0.002	12.55	0.017–0.027	0.052–0.064	17.66–18.55	
H_s	25	0.1	2×10^{-5}	4.21	0.004–0.009	0.010–0.020	56.13–89.37	
H_{b_1}	25	0.1	2×10^{-5}	4.21	0.011–0.021	0.040–0.052	21.56–22.45	0.165
H_{b_2}	25	0.1	2×10^{-5}	4.21	0.012–0.022	0.063–0.077	11.87–12.76	
H_s	16	0.01	0.001	12.53	0.002–0.004	0.004–0.009	125.88–219.63	
H_{b_1}	16	0.01	0.001	12.53	0.008–0.014	0.027–0.035	32.00–35.60	0.531
H_{b_2}	16	0.01	0.001	12.53	0.014–0.024	0.047–0.058	19.03–19.93	
H_s	16	0.01	0.002	12.53	0.003–0.005	0.005–0.010	122.05–203.81	
H_{b_1}	16	0.01	0.002	12.53	0.010–0.016	0.030–0.038	29.80–32.57	0.400
H_{b_2}	16	0.01	0.002	12.53	0.014–0.024	0.050–0.061	17.67–18.51	
H_s	16	0.01	0.01	12.55	0.003–0.005	0.005–0.010	122.05–203.81	
H_{b_1}	16	0.01	0.01	12.55	0.010–0.016	0.030–0.038	29.80–32.57	0.397
H_{b_2}	16	0.01	0.01	12.55	0.014–0.024	0.050–0.061	17.67–18.51	
H_s	16	0.1	10^{-4}	4.21	0.004–0.010	0.010–0.023	49.14–90.37	
H_{b_1}	16	0.1	10^{-4}	4.21	0.015–0.029	0.051–0.067	17.27–18.58	0.319
H_{b_2}	16	0.1	10^{-4}	4.21	0.015–0.027	0.086–0.103	8.74–9.25	
H_s	16	0.1	2×10^{-5}	4.21	0.002–0.006	0.006–0.013	84.23–144.92	
H_{b_1}	16	0.1	2×10^{-5}	4.21	0.006–0.010	0.032–0.038	24.15–25.40	0.088
H_{b_2}	16	0.1	2×10^{-5}	4.21	0.009–0.018	0.048–0.059	16.03–16.99	

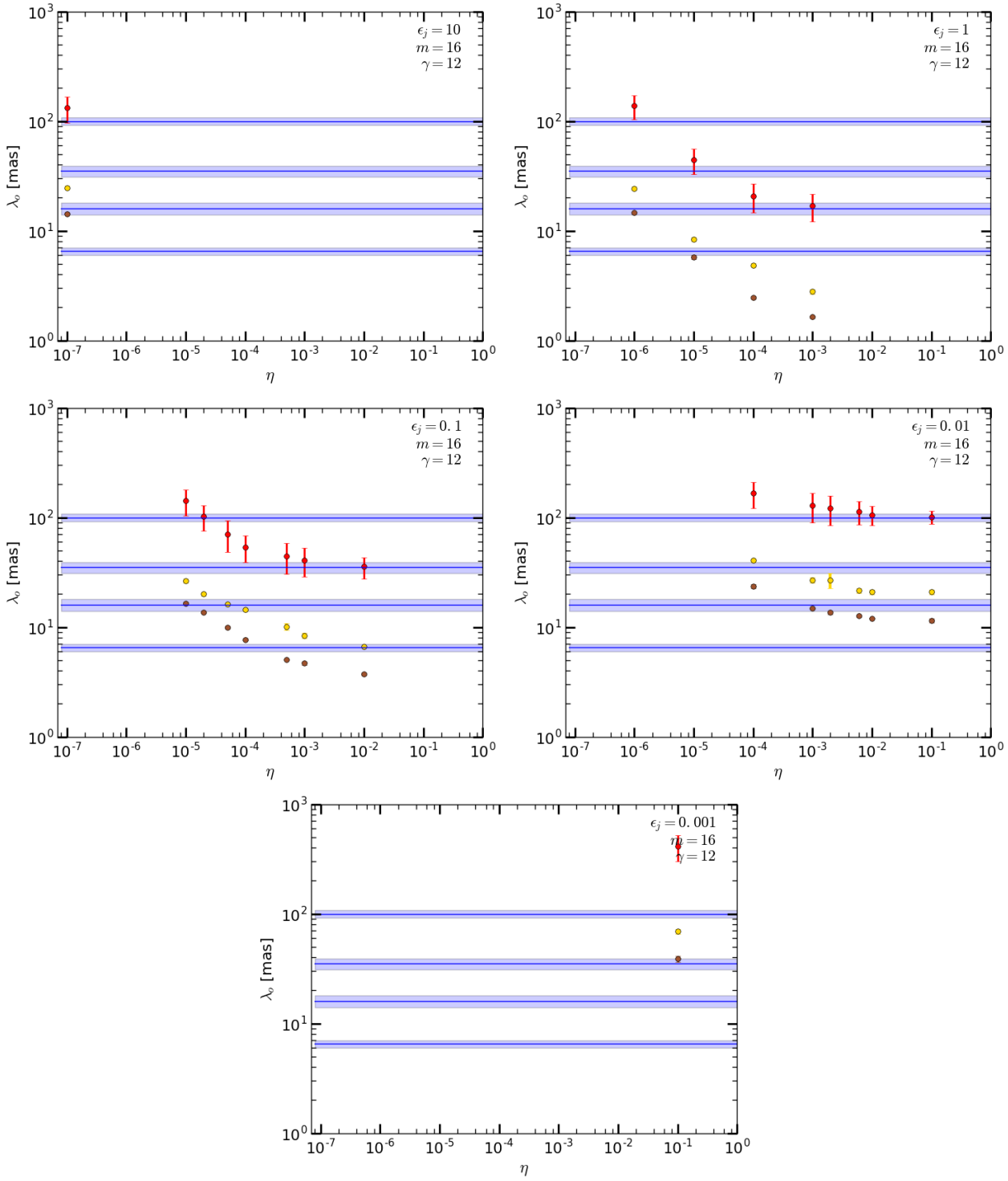

Fig. A.1. Corresponding observed wavelengths from the calculations for $m = 16$. The color scale and the meaning of the horizontal lines are the same as used in Fig. 5. The corresponding jet internal energy for each plot is written in the figure.

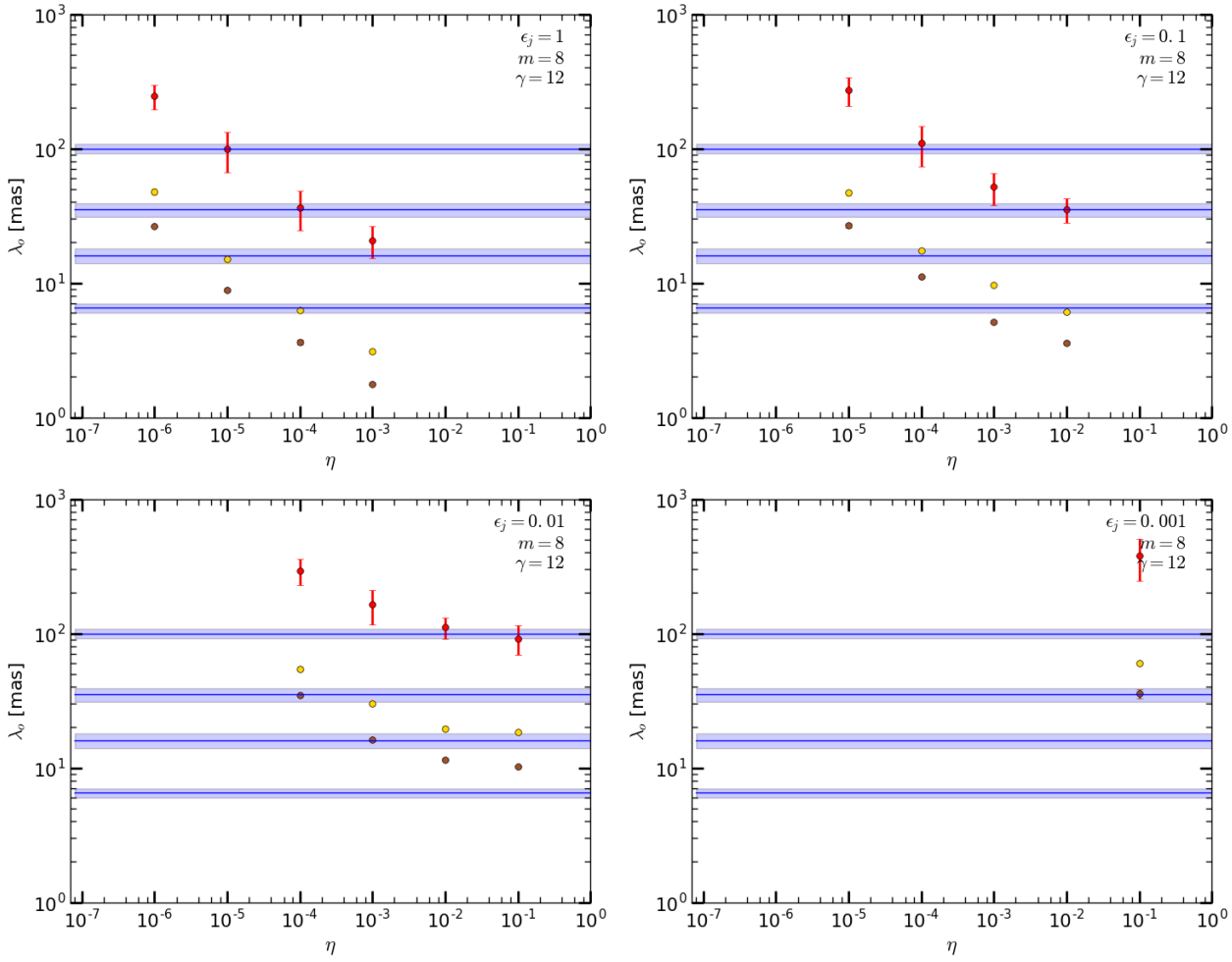

Fig. A.2. Corresponding observed wavelengths from the calculations for $m = 8$. The color scale and the meaning of the horizontal lines are the same as used in Fig. 5. The corresponding jet internal energy for each plot is written in the figure.

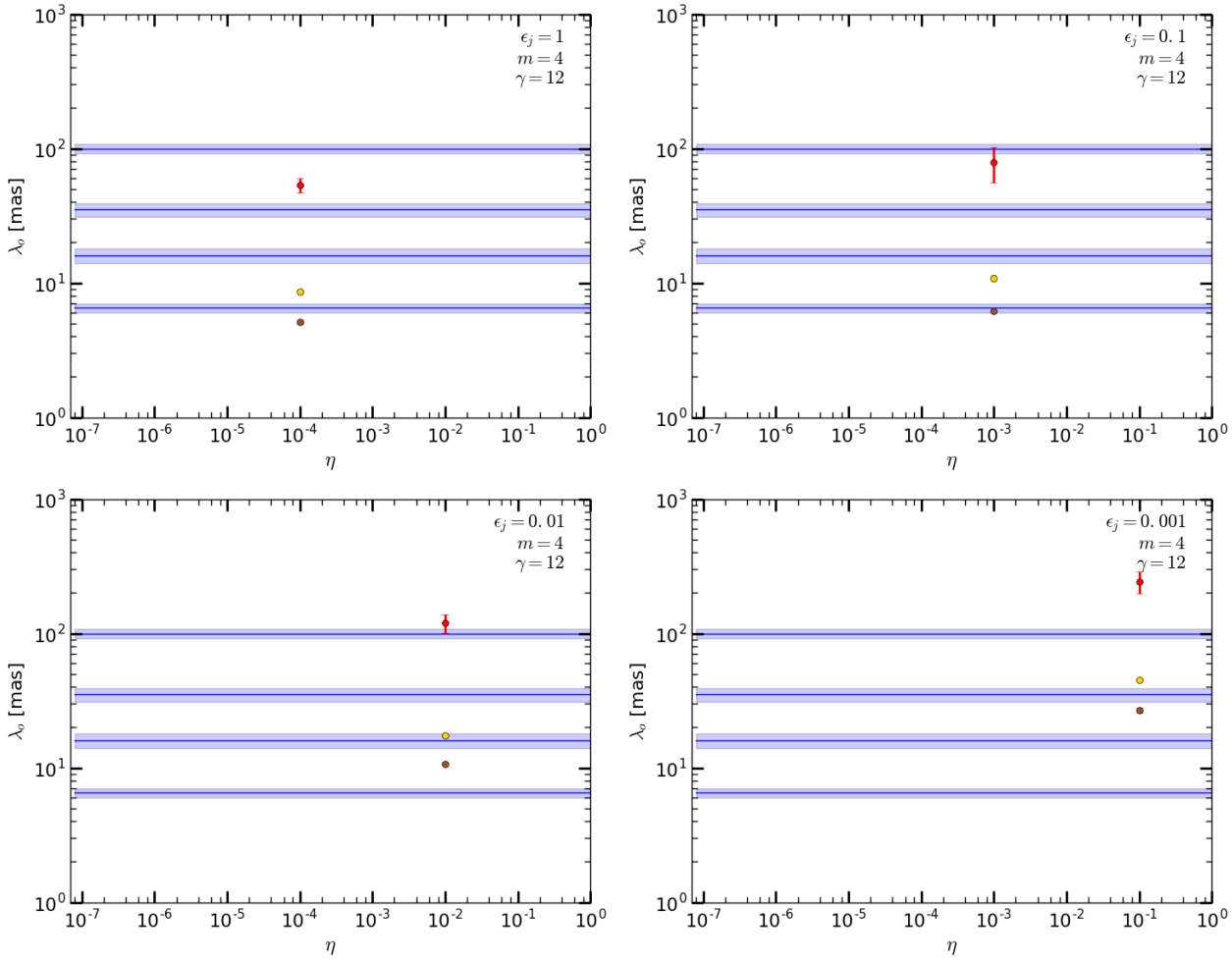

Fig. A.3. Corresponding observed wavelengths from the calculations for $m = 4$. The color scale and the meaning of the horizontal lines are the same as used in Fig. 5. The corresponding jet internal energy for each plot is written in the figure.

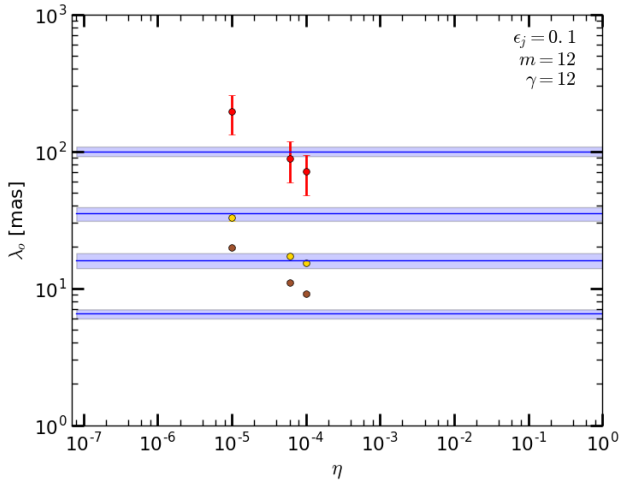

Fig. A.4. Corresponding observed wavelengths from the calculations for $m = 12$. The color scale and the meaning of the horizontal lines are the same as used in Fig. 5. The corresponding jet internal energy for each plot is written in the figure.

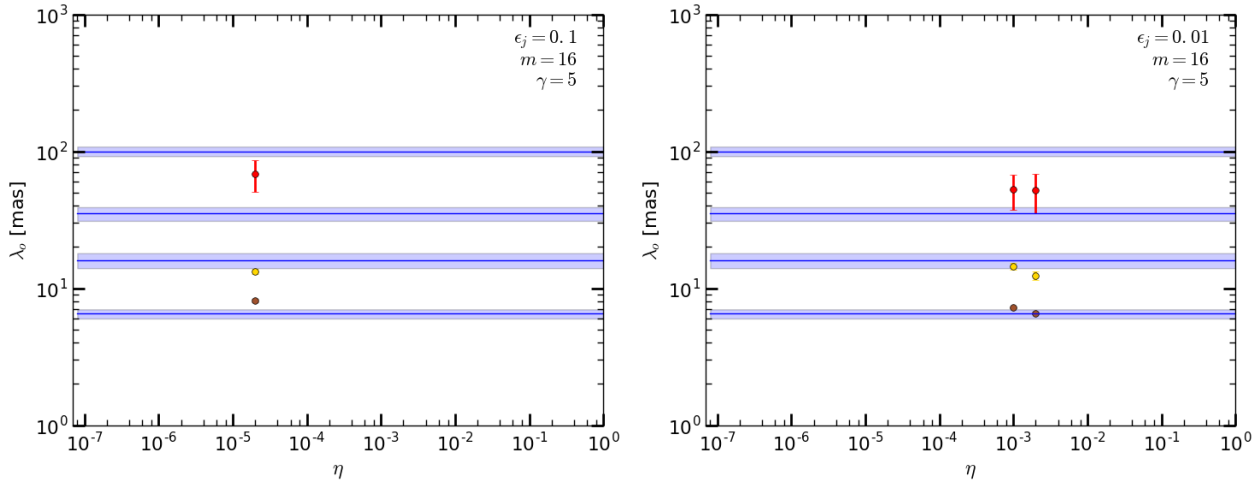

Fig. A.5. Corresponding observed wavelengths from the calculations for $m = 16$ and $\gamma = 5$. The color scale and the meaning of the horizontal lines are the same as used in Fig. 5. The corresponding jet internal energy for each plot is written in the figure.

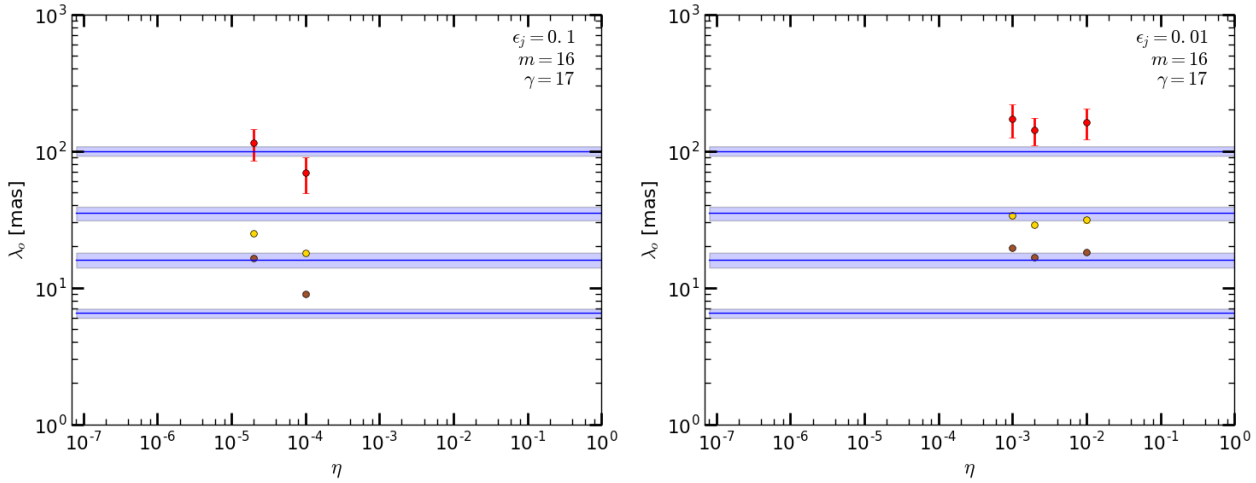

Fig. A.6. Corresponding observed wavelengths from the calculations for $m = 16$ and $\gamma = 17$. The color scale and the meaning of the horizontal lines are the same as used in Fig. 5. The corresponding jet internal energy for each plot is written in the figure.

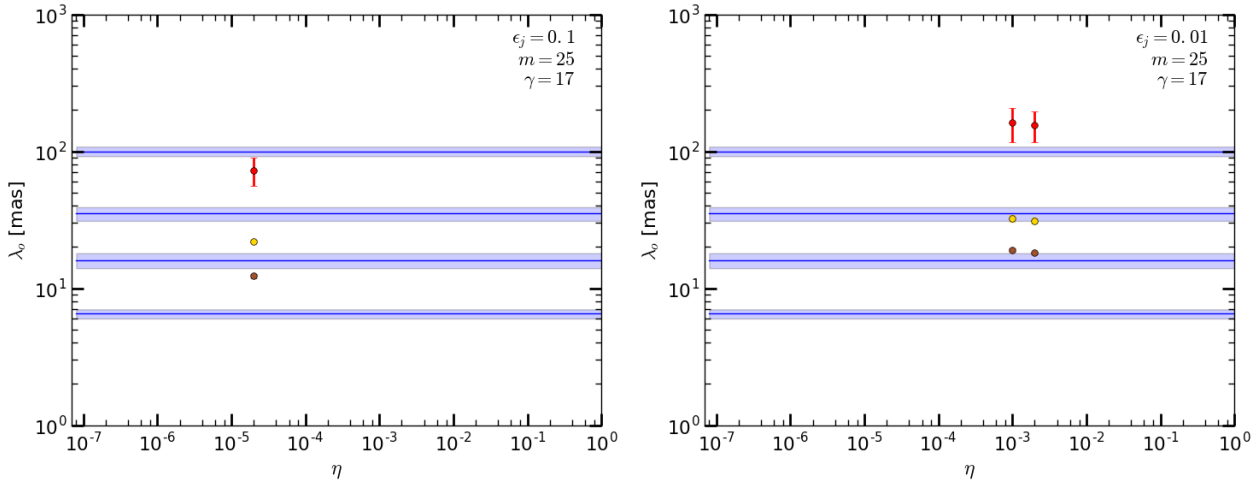

Fig. A.7. Corresponding observed wavelengths from the calculations for $m = 25$ and $\gamma = 17$. The color scale and the meaning of the horizontal lines are the same as used in Fig. 5. The corresponding jet internal energy for each plot is written in the figure.